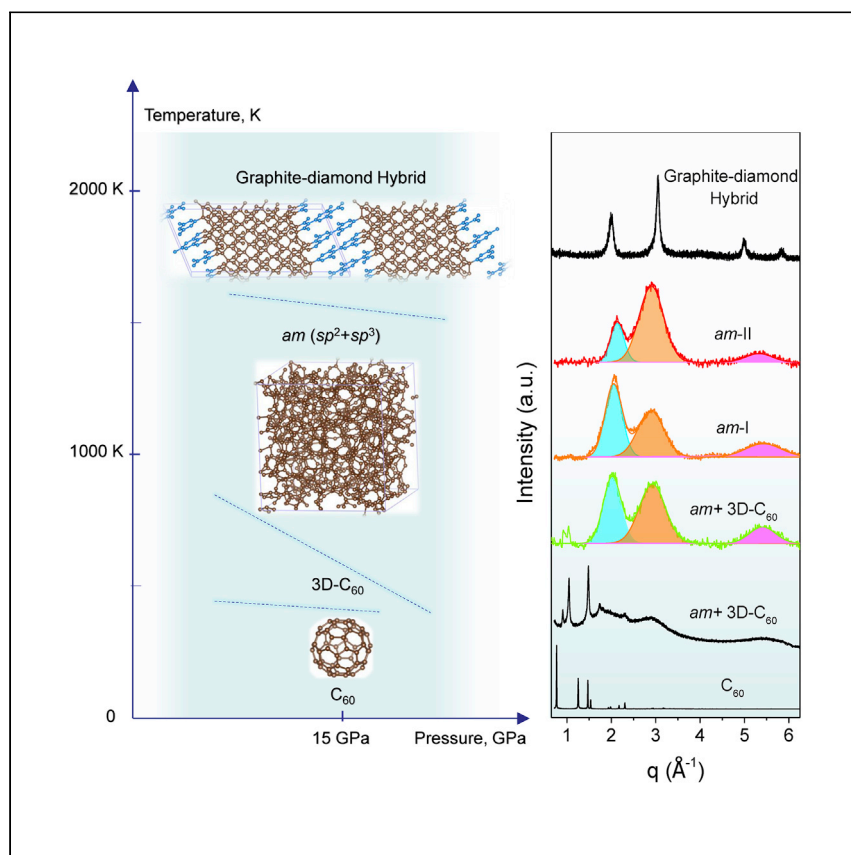## Article

Narrow-gap, semiconducting, superhard amorphous carbon with high toughness, derived from C_{60} fullerene

HPSTAR
1327-2021

Shuangshuang Zhang, Yingju Wu, Kun Luo, ..., Dongli Yu, Bo Xu, Yongjun Tian

zzhao@ysu.edu.cn (Z.Z.)
alexander.soldatov@ysu.edu.cn (A.V.S.)
fhcl@ysu.edu.cn (Y.T.)

Highlights

Narrow-gap, superhard amorphous carbon materials are formed from compressing C_{60}

Two distinct, short-range microstructures in the amorphous carbon are recognized

A long-missing structural transformation model is developed from C_{60} to amorphous carbon

Synthesis of amorphous carbon from fullerene C_{60} under extreme pressure is often not well understood, which impedes further progress in the materials design. Zhang et al. propose a long-missing structural transformation model from C_{60} to amorphous carbon and raise the future development of amorphous carbon with controllable disorder.

Article

Narrow-gap, semiconducting, superhard amorphous carbon with high toughness, derived from C$_{60}$ fullerene

Shuangshuang Zhang,[1,8] Yingju Wu,[1,8] Kun Luo,[1,2,8] Bing Liu,[1,8] Yu Shu,[1] Yang Zhang,[1,2] Lei Sun,[1] Yufei Gao,[1,2] Mengdong Ma,[1] Zihe Li,[1] Baozhong Li,[1] Pan Ying,[1,2] Zhisheng Zhao,[1,9,*] Wentao Hu,[1] Vicente Benavides,[3,4] Olga P. Chernogorova,[5] Alexander V. Soldatov,[1,6,7,*] Julong He,[1] Dongli Yu,[1] Bo Xu,[1] and Yongjun Tian[1,*]

SUMMARY

New carbon forms that exhibit extraordinary physicochemical properties can be generated from nanostructured precursors under extreme pressure. Nevertheless, synthesis of such fascinating materials is often not well understood. That is the case of the C$_{60}$ precursor, with irreproducible results that impede further progress in the materials design. Here, the semiconducting amorphous carbon, having band gaps of 0.1–0.3 eV and the advantages of isotropic superhardness and superior toughness over single-crystal diamond and inorganic glasses, is produced from fullerene at high pressure and moderate temperatures. A systematic investigation of the structure and bonding evolution is carried out with complementary characterization methods, which helps to build a model of the transformation that can be used in further high-pressure/high-temperature (high p,T) synthesis of novel nano-carbon systems for advanced applications. The amorphous carbon materials produced have the potential of accomplishing the demanding optoelectronic applications that diamond and graphene cannot achieve.

INTRODUCTION

Given the structural diversity of allotrope forms (graphite, graphene, diamond, fullerene and nanotubes, nano-onions, etc.) that carbon exhibits, it is likely the most intriguing element of the periodic table. Bonding varieties, such as sp, sp^2, and sp^3 hybridization, manifest as distinct electronic and mechanical properties. For example, diamond has a three-dimensional (3D) structure comprising rigid sp^3 bonds, whereas graphite is a stack of weakly bonded (by Van der Waals forces) graphene layers with honeycomb lattices of covalently bonded sp^2 carbons. Consequently, diamond is an extremely hard insulator, whereas graphite is a soft semimetal. Free-standing, single-layer graphene is mechanically flexible with ultra-high carrier mobility. However, the gapless character of graphene makes it unsuitable for on/off operations in field-effect transistors, which hinders its utility in next-generation electronic devices.[1] Considerable efforts have been made to open a sizable band gap in graphene via doping, adatoms, and quantum confinement on nanometer scale, as well as from symmetry breaking by applying an external electric field or high pressure.[2,3] Thus far, the band gap in bilayer graphene attained under ambient conditions can reach several hundreds of mega electron-volts, making it a potential candidate for use in electronic devices.[4]

[1]Center for High Pressure Science (CHiPS), State Key Laboratory of Metastable Materials Science and Technology, Yanshan University, Qinhuangdao, Hebei 066004, China

[2]Key Laboratory of Microstructural Material Physics of Hebei Province, School of Science, Yanshan University, Qinhuangdao 066004, China

[3]Department of Engineering Sciences and Mathematics, Luleå University of Technology, SE-97187 Luleå, Sweden

[4]Department of Materials Science, Saarland University, Campus D3.3, 66123 Saarbrücken, Germany

[5]Baikov Institute of Metallurgy and Materials Science, Moscow 119334, Russia

[6]Center for High Pressure Science and Technology Advanced Research, Shanghai 201203, China

[7]Department of Physics, Harvard University, Cambridge, MA 02136, USA

[8]These authors contributed equally

[9]Lead contact

*Correspondence: zzhao@ysu.edu.cn (Z.Z.), alexander.soldatov@ysu.edu.cn (A.V.S.), fhcl@ysu.edu.cn (Y.T.)

https://doi.org/10.1016/j.xcrp.2021.100575

Carbon forms with two or more hybrid states exhibiting unusual electronic and mechanical properties through the combination of the advantages of each state, and those forms are highly sought after.[5–8] Most typical examples are the sp^2-sp^3 amorphous carbon films, such as (hydrogenated) amorphous carbon (a-C(:H)) and (hydrogenated) tetrahedral amorphous carbon (ta-C(:H)), with thicknesses of a few hundred nanometers, which can be produced by various deposition techniques, including ion-beam deposition, ion-assisted sputtering, cathodic-vacuum arc, pulsed-laser deposition, and plasma-enhanced chemical-vapor deposition.[5,7,9,10] Amorphous carbon films are semiconductors with outstanding mechanical-tribological properties (superhigh hardness and excellent wear resistance) and are widely used as superior protective coatings and in optoelectronic applications.[5] However, reducing the band gap of amorphous carbon films to less than 0.4 eV experimentally is challenging,[5,10] and otherwise, the conductive films have significantly reduced mechanical properties.[11] In addition, understanding the electronic behavior of amorphous carbon materials remains a challenge. There are some contradictions between the photoconductivity and doping behavior of ta-C and the high measured density of spins, and the conditions under which a gap opens in the π states are also not well understood.[9] Moreover, high internal stresses accompany film manufacturing, leading to poor adhesion to the substrate and weakening the durability and service life of the films and also preventing synthesis of those materials in bulk form.[12] Nevertheless, one solution to this major problem may be through the use of other manufacturing protocols, such as high-pressure techniques. Indeed, much hope and enthusiasm was brought about by scientific reports highlighting the extraordinary properties of disordered carbon systems derived from various sp^2 carbon precursors, including fullerene[13–15] and glassy carbon[16,17], under high pressure. For example, a class of lightweight, amorphous carbon bulk materials, with robust elastic recovery after indentation, electro-conductivity, and high strength and hardness, were recently obtained by compressing glassy carbon at pressures of 5–25 GPa and temperatures of $\leq$1,200°C.[16,18] These materials consisted of disordered multilayer graphene sheets, which were locally buckled or linked by sp^3 carbon bonds, resulting in the remarkable combination of mechanical properties they exhibited. Another class of superelastic, hard amorphous carbon materials was built from disordered, nano-sized graphene clusters and were produced by crushing C_{60} molecules at pressures of 5–8 GPa and temperatures of >800°C.[14,19] It was proposed that a correlation between the graphene nanocluster orientation and the crystalline structure of the fullerene parent endowed the material with unique mechanical properties.[14] Similar to a-C(:H) and ta-C(:H) coatings, those materials provided enhanced tribological properties when used as additives in composites, with a 40 to 140-fold increase in those properties and a 2-fold decrease in the wear resistance and friction coefficient, respectively.[20]

Increasing the synthesis pressure to 12–15 GPa brought additional exciting results upon the C_{60} transformation. Some reports claimed that the synthesized amorphous carbon materials with ultrahigh hardness could even scratch single-crystal diamond.[15,21] However, reports on the mechanical properties of these amorphous carbon materials were controversial and/or inconclusive.[15,21,22] For example, it was argued that amorphous carbon synthesized at 13 GPa, and 900–1,830 K is able to scratch a diamond crystal surface, thus possessing hardness exceeding that of a diamond.[15] The hardness was evaluated according to a sclerometer test method and yielded values as high as 170–300 GPa.[21] However, subsequent hardness measured by the indentation method on samples produced at similar conditions was only 45–87 GPa.[22,23] In addition, only occasional and insufficient studies have been conducted regarding the electrical and optical properties of amorphous carbon materials,[24]

and no direct characterization of the structural transformations on the nanoscale level has been performed. Furthermore, no study investigating their dependence on synthesis pressure and temperature (p,T) has been conducted to date. Differences in the synthesis p,T and process protocol (rate of temperature and pressure rise/drop and the holding time at a target p,T), as well as the level of the hydrostatic pressure in the previous experiments, may hinder a proper comparison of the data and be the cause for the poor reproducibility of the samples produced.[13] Consequently, a general understanding of the synthesis process of amorphous carbon materials is incomplete. Only one valuable attempt to model the behavior of C_{60} precursors into amorphous carbon materials produced at high p,T was conducted by Brazhkin et al.[25] That study proposed that 3D polymerization of C_{60} is two-stage process, and the initial polymerization occurs via the 2 + 2 cycloaddition mechanism, followed by a substantial level of polymerization with four or more covalent bonds (sp^3 atoms) bridging the neighboring buckyballs. Nevertheless, that effort was limited to the formation of 3D-C_{60} polymers and, to our knowledge, no structural models of the fullerene transformation into various amorphous carbon materials have been proposed in addition to a recent theoretical, simulation work.[26] This knowledge gap strongly impedes materials design and their prospective practical applications. Therefore, this study attempts to fill that knowledge gap by bringing to use a broad array of complimentary analytical tools to characterize a wide range of the physical properties of the amorphous carbon materials recovered after the high p,T synthesis.

Herein, we present the results of a systematic study on C_{60} fullerene transformation into amorphous carbon materials at 15 GPa and at temperatures exceeding the threshold of the buckyball integrity. The synthesis pressure is slightly above the pressure level (12–13 GPa) at which the most interesting and controversial results were previously obtained.[13,21,22,27] Various analytical tools, including X-ray diffraction (XRD), Raman spectroscopy, high-resolution transmission electron microscopy (HRTEM), and electron energy-loss spectroscopy (EELS) were used to assess the key structural evolutionary stages. Using HRTEM observations, subtle differences in the structure were identified. The mechanical properties of amorphous carbon materials are studied using three independent methods. Specifically, Vickers, Knoop, and nano-indentation techniques were used to verify the results, revealing a diamond-like hardness of the synthesized materials and fracture toughness comparable to that of Co-doped polycrystalline diamond.[28] We find that the amorphous carbon materials produced are semiconductors with band gaps of only ~0.1–0.3 eV, as determined by Fourier transform infrared-attenuated total reflectance (FTIR-ATR) spectra and temperature-dependent electrical resistivity. These narrow-gap amorphous carbon semiconductors with superior mechanical properties may have unique photoelectric applications, such as in the mid-far-infrared fields (Video S1).

RESULTS AND DISCUSSION

Characterization of microstructure

The XRD patterns in Figure 1A show the phase transition of C_{60} after high-pressure treatment at 15 GPa and different temperatures ranging from 550°C to 1,200°C. The raw C_{60} fullerene first transformed into 3D-C_{60}, accompanied by a certain degree of amorphization at the relatively low-synthesis temperature of T = 550°C, with sample 1 following similar results, as previously reported.[21,29] The amorphization was almost finished at T = 700°C (sample 2). Amorphous carbon materials 3 and 4 (denoted as *am*-I and *am*-II) were quenched at 800°C and 1,000°C, respectively, and possessed
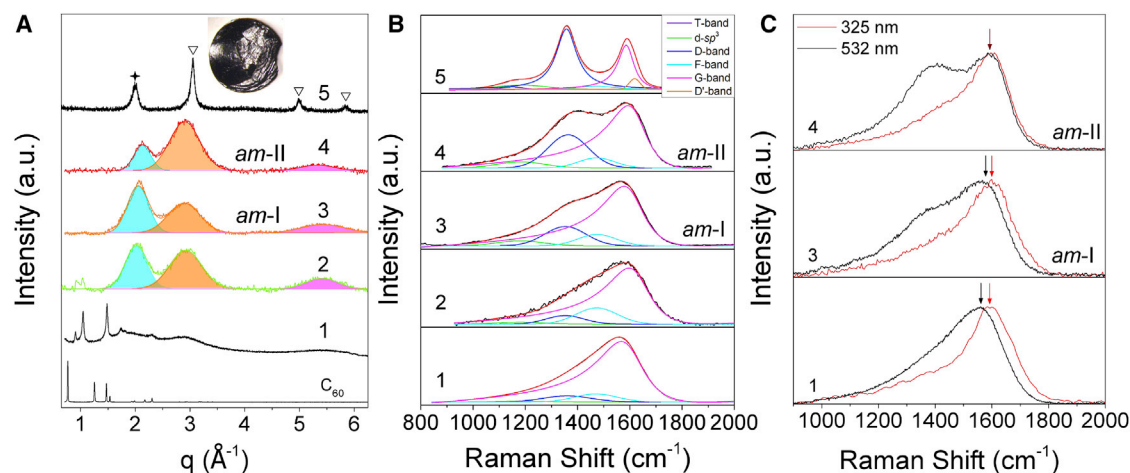
Figure 1. XRD patterns and Raman spectra of resulting carbon materials measured at ambient conditions

Numbers 1–5 represent the resulting carbon materials from the compression of C_{60} at 15 GPa and various temperatures at 550°C, 700°C, 800°C, 1,000°C, and 1,200°C. All recovered samples are black blocks, and the inset in (A) is a photo of *am*-I with diameter of ~1.6 mm.

(A) The XRD patterns indicate that C_{60} first transformed to 3D-C_{60} at high pressure and high temperature, began amorphization, and finally transformed into a compressed graphite-diamond composite. The *am*-I and *am*-II had three broad diffraction peaks with similar positions at q = ~2.1, ~3.0, and ~5.4 Å^{-1}, but at different intensities. The stars and triangles indicate the reflections of the compressed graphite and diamond, respectively.

(B) Raman spectra of samples 1–5 were collected using 532-nm laser excitation. Peak fitting of the Raman spectra was conducted according to the Ferrari and Robertson model,[33,34,35] with a position specific to our system. Peak assignments are listed in Table S1, and the peak decomposition rates of the spectra are summarized in Table 1.

(C) Comparison of Raman spectra excited by a 325- and 532-nm laser. The comparison shows a dispersion of the G-band in samples 1, 3, and 4, indicating the presence of different types of disordered components in the microstructure. All Raman data were background free.

three main, broad diffraction peaks around a structural factor of q = ~2.1, ~3.0, and ~5.4 Å^{-1}, with close positions but different intensities, especially for the first two peaks. There were some differences between the synthesized amorphous carbon materials and those previously synthesized from C_{60} under relatively lower p,T conditions (12.5 GPa, 500–700°C).[30] The residual diffraction peak near ~1.5 Å^{-1} for C_{60} was observed in the latter samples,[30] suggesting incomplete amorphization. The peak at ~2.1 Å^{-1} corresponded to the average interlayer spacing (d = ~2.99 Å) of the compressed, disordered, graphite-like component in the amorphous carbon, similar to sp^2-sp^3-compressed glassy carbon,[16,31] and compressed graphite formed after non-hydrostatic pressurization of C_{60} at ambient temperatures.[32] The other two broad peaks at ~3.0 and ~5.4 Å^{-1} in the amorphous carbon materials corresponded to d = ~2.09 and 1.16 Å, respectively. There were differences for d = 2.06, 1.26, and 1.08 Å of diamond (111), (220), and (311) planes. When the synthesis temperature increased from 700°C to 1,000°C, the diffraction peak at ~2.1 Å^{-1} gradually narrowed and slightly shifted to the right, indicating that the layers in the compressed, disordered, graphite-like component were more regular and the average interlayer spacing was smaller. In addition, the ~2.1 Å^{-1} peak intensity initially increased and then decreased. This abnormal change was possibly related to the complete fragmentation of 3D-C_{60}, re-polymerization of small graphene fragments with different sizes and shapes and the further development of graphite-like and diamond-like, disordered components in the microstructure, which was supported by the HRTEM observations of microstructure changes during the phase transformation. When the synthesis temperature increased to 1,200°C, the recovered sample 5 showed four sharp diffraction peaks, implying crystallization. The first peak at q = ~2.0 Å^{-1} corresponded to the previously so-called compressed graphite,[31,32] and the last three peaks at ~3.02, ~4.99, and ~5.84 Å^{-1} correspond to the diamond reflections of (111), (220), and (311), respectively.

Figures 1B, 1C, and S1–S3 show the Raman spectra of the recovered samples. The position of the Raman modes in the raw C_{60} spectrum (Figure S1) was in good agreement with data in the literature, and the strongest peak at 1,469 cm^{-1} corresponded to the A_{2g} pentagon-pinch mode in monomeric fullerene.[36] After high p,T treatment, the Raman spectra showed profound changes in the recovered materials. Samples 1–3 revealed a very broad, asymmetric feature between 1,200 and 1,800 cm^{-1} with the highest intensity and between 1,500 and 1,600 cm^{-1}, which is typical for highly disordered or amorphous carbon systems. In addition, the G-band in the spectrum was characteristic of vibrational modes, indicating sp^2-bonded carbon atoms. The Raman spectrum of sample 4 exhibited a developed shoulder in the low-frequency range in the broad main feature of the spectrum. This shoulder grew in intensity with further increases in synthesis temperature, and in sample 4, it reached the intensity of the main feature at ∼1,600 cm^{-1}. A significant change in the Raman spectrum profile was demonstrated in sample 5, which was synthesized at the highest experimental temperature of 1,200°C. Two separate, narrower peaks than the corresponding features in the spectrum 4 were assigned to the D and G vibrational bands of the honeycomb structure of graphene. Specific information about the disordered carbon structures was obtained from the peak decomposition of the Raman spectra, along with their assignments and analysis. Table S1 summarizes the peak assignments used in our model: the G-band[33,34,37,38] (E_{2g} Raman mode) characteristics of various structural forms of sp^2-bonded carbon atoms; the vibrational modes of 5-fold (F-band)[14,39,40] and 7-fold[14,39,40] aromatic rings relevant to our system, given the precursor material C_{60}; the D-band[14,33,34,37,38,41] describing the "breathing" vibrational mode of 6-fold (hexagonal) aromatic "rings," which is also the A_{1g} Raman mode in graphene, associated with defects, as is the other double-resonant, defect-related graphene mode D';[14,33,34,37,38] and finally, the characteristic Raman features of sp^3-bonded carbons: T-band,[34] the hallmark of disordered, nearly pure sp^3-bonded (ta-C(:H) carbon systems and nano-polycrystalline diamond; and a peak reported for amorphous sp^2-sp^3 carbon systems,[42,35] which we term, here, as the "disordered-sp^3" (d-sp^3) peak.

A Breit-Wigner-Fano (BWF) function, the asymmetric ("stretched") Lorentzian, is suitable for description of the G-band that is the contribution from sp^2-bonded carbon atoms in amorphous and disordered carbon systems.[33,34,37,38] Because of the complexity and structural inhomogeneity of the sp^2 component, which may include various structural units present simultaneously in the system—linear chains, fused aromatic rings, and, as a specific case of the latter, small clusters/stacks of fused hexagonal rings—and a few-layer graphene "seeds." Thus, we used the BWF function for the peak decomposition of the highly disordered carbon systems studied in this work. Deviation of the BWF from the Lorentzian peak shape or the degree of BWF asymmetry was mathematically described by the so-called Q_{BWF} factor, in which a smaller $1/Q_{BWF}$ value indicates less asymmetry in the BWF peak, and an infinite Q_{BWF} factor (zero $1/Q_{BWF}$) corresponds to a Lorentzian peak shape is and asymptote of the BWF function. Gaussian functions were used for fitting the F, D, d-sp^3, and 7-ring-derived Raman peaks.

The peak decomposition of the Raman spectra is displayed in Figure 1B, and more details are shown in the tables within Figures S2 and S3. Summaries of the fitted results are presented in Table 1. For these spectra, the Q_{BWF} factor was directly associated with the sp^3-bonded carbon atom content in the system. Because Raman spectra were composed of numerous peaks, the Q_{BWF} values obtained were not directly associated with sp^3 carbon content. Nevertheless, from a qualitative comparison of the results, we determined that higher/lower sp^3 carbons fraction in

Table 1. Summary of the Raman spectra analysis (the key parameters derived from the spectra): G-band peak position, width (FWHM) and shape (asymmetry factor Q_{BWF}), $1/Q_{BWF}$ parameter, D/G(BWF) peak-area ratio, and the size of the coherent scatterers (L_a)

Temperature (°C)	G-band position (cm^{-1})	G-band width (FWHM)	D/G (peak area), %	Q_{BWF}	$1/Q_{BWF}$	Cluster size L_a(nm)
550	1,567	230	0.07	−3.57	−0.28	<2
700	1,577	218	0.06	−3.70	−0.27	<2
800	1,578	210	0.10	−3.45	−0.29	<2
1,000	1,593	196	0.38	−3.23	−0.31	<2
1,200	1,586	74	1.89	−12.5	−0.08	10 ± 2

different samples result in lower/higher Q_{BWF} values, respectively. In the Raman spectra shown in Figure S2, the shape of the BWF peak gradually changed with the synthesis temperature. For example, the Q_{BWF} factor derived from the BWF peak decreased with increasing synthesis temperature, from 550°C in sample 1 (Figure S2A) to 1,200°C in sample 5 (Figure S3B). This implies an increase in the sp^3 carbon fraction. The D-band was characteristic of hexagonal rings in the system. Although visually unnoticeable in the spectra collected from samples 1 and 2 synthesized at lower temperatures (550°C and 700°C, respectively), the D-band intensity gradually increased with synthesis temperature. This first manifested in the form of a shoulder on the low-frequency side of the G-band (BWF peak) and grew into a well-defined separate peak with greater intensity than the G-band, implying the presence of multi-layered graphene (MLG) in the system. The Q_{BWF} factors and the $1/Q_{BWF}$ parameters derived from the Raman spectra reflect the dependence on the synthesis temperature of the sample (Table 1). Interestingly, the $1/Q_{BWF}$ parameter value (−0.08) of the BWF/G-band peak, in sample 5 (1,200°C) was similar to the one reported for G-band in graphene.[43] The BWF peak shape with the $1/Q_{BWF}$ parameter approached the symmetrical function (Lorentzian peak shape).

Another important conclusion about the structural evolution regarding the sp^2 carbon components can be drawn from the D/G peak-area ratio, in which the fraction of sp^2 carbons incorporated in the hexagonal rings corresponds with the total number of sp^2 carbons in the system. The D/G peak-area ratio increased from 0.1 in am-I (800°C) to 0.38 in am-II (1,000°C), reaching a final value of 1.89 in the nanographene/nanographite (1,200°C). This Raman spectra evolution reflected the gradual growth of hexagonal rings in the system at the expense of other sp^2-carbon-based structural units, until all of the sp^2-bonded carbon atoms were associated with hexagons in the pure hexagonal ring-based (honeycomb) structure. Thus, the nanographene/nanographite phase concluded the structural evolution. The top panel in Figure S4 illustrates this process through the dependence of G-band peak full width at half maximum (G-FWHM) and the D/G peak-area ratio on the synthesis temperature. Even though the G-FWHM decreased as a function of temperature, it remained very broad (>200 cm^{-1}) until the temperature reached 1,200°C. The broad G-bands corresponded to a coherent size (<2 nm) of the Raman scatterers (fused hexagons/nanographene clusters). Samples 1–4 (550–1,000°C) were thus placed in Stage II of the Ferrari and Robertson ternary phase diagram/graphene amorphization/growth pathway.[33,34] As the synthesis temperature increased from 700°C to 1,000°C, the system moved from Stage II toward Stage I (Figure S4, bottom panel). Additional evidence of the dominance of the hexagonal rings among the nanostructural units built from the sp^2 atoms at a certain stage of the system evolution comes from comparison of the Raman spectra collected with different laser excitation levels. Figure 1C displays a clear blue shift in the BWF (G-band) peak in the spectrum acquired with a 325-nm (UV) laser,

compared with the one collected with a 532-nm (visible) laser for samples 1 and 3 (G-band dispersion). By contrast, sample 4 exhibited no G-band dispersion (the BWF peaks coincided). The G-band dispersion originated from a variety of sp^2-carbon-based structural units (chains, different fused aromatic rings, and small clusters) present in the amorphous carbon system. This caused the resonant behavior of the G-band because different structural units are in resonance at different laser excitation levels, causing the G-band peaks to appear at different frequencies. Consequently, the dispersion of the G-band verified the high structural inhomogeneity in the system, and there was no preference or dominance of certain structural species. For example, in samples 1 and 3, many structural units (short chains, pentagons, hexagons, and heptagons) formed on the collapse of fullerene cages, whereas hexagons did not dominate. However, the lack of dispersion in sample 4 indicated that the hexagon-based structural elements dominated in the system. In addition, sp^2 carbons had low Raman cross-sections for UV laser excitation, which was corroborated by the low intensity of the UV Raman spectra in the D-band energy range, as shown in Figure 1C. Instead, there was a gradual rise of the D-band in the Raman spectra acquired with a 532-nm laser, indicating that the number of hexagons increased or the graphene grew in the system with increased temperature.

Finally, the Raman spectra at 1,200°C were associated with Stage I graphene amorphization or growth trajectory from the D/G (BWF) peak-area ratio and the G-band peak position, width, and peak shape (Q_{BWF} factor value), as shown in Table 1. This was related to the establishment of the nanoclustered MLG/nanographite phase in the system. Nanographene cluster sizes (L_a) were estimated from the G-band FWHM[44] and the D/G peak area ratio (A_D/A_G)[45] at 10 ± 2 nm and 9 ± 2 nm, respectively.

HRTEM was used to observe the microstructure differences in the quenched carbon samples directly (Figures 2 and S5). Figure 2A shows the intermittent periodic patterns in sample 1, indicating that local amorphization was caused by the partial collapse of the 3D-C_{60} structure. In addition, the corresponding selected area electron diffraction (SAED) (Figure S5A) and fast Fourier transform (FFT) patterns showed the joint broadened amorphous halo and crystalline spots. For *am*-I obtained at a higher synthesis temperature, a completely disordered structure was observed, and two types of short-range microstructures were visible inside. One exhibited small and disordered, fingerprint-like, curved fragments with graphite-like interlayer spacing ($d_{average}$ = 0.368 nm) (blue box area in Figure 2B). The other structure appeared more compact with shorter spacing because of the sp^3 linkages in this area (red box area in Figure 2B). The corresponding SAED (Figure S5B) and FFT patterns showed only amorphous halo features. With further increases in synthesis temperature, the previously fingerprint-like, small, curved fragments in *am*-I combined into more-ordered and regular MLG nanoclusters in *am*-II, with reduced interlayer spacing ($d_{average}$ = 0.322 nm) and orientation (blue box area in Figure 2C). Thus, the dense, disordered regions were enlarged in *am*-II (red box area in Figure 2C). The corresponding FFT patterns of the marked HRTEM areas indicated that, unlike the obvious inner halo of the disordered and layered regions, the interlayer diffraction halo decreased until it almost disappeared in the dense regions from *am*-I to *am*-II (Figures 2B and 2C). This was also observed in their SAED patterns (Figures S5B and S5C). Thus, both *am*-I and *am*-II exhibited long-range disordered structures, but with different short-range orders. In sample 5, which was synthesized at a higher temperature, the dense, disordered parts in *am*-II transformed into nanodiamond (with $d_{(111)}$ = 0.206 nm), and compressed nanographite (with $d_{average}$ = 0.317 nm) transformed from the parts composed of more-ordered MLG nanoclusters in *am*-II were also clearly visible in the composite (Figure 2D).
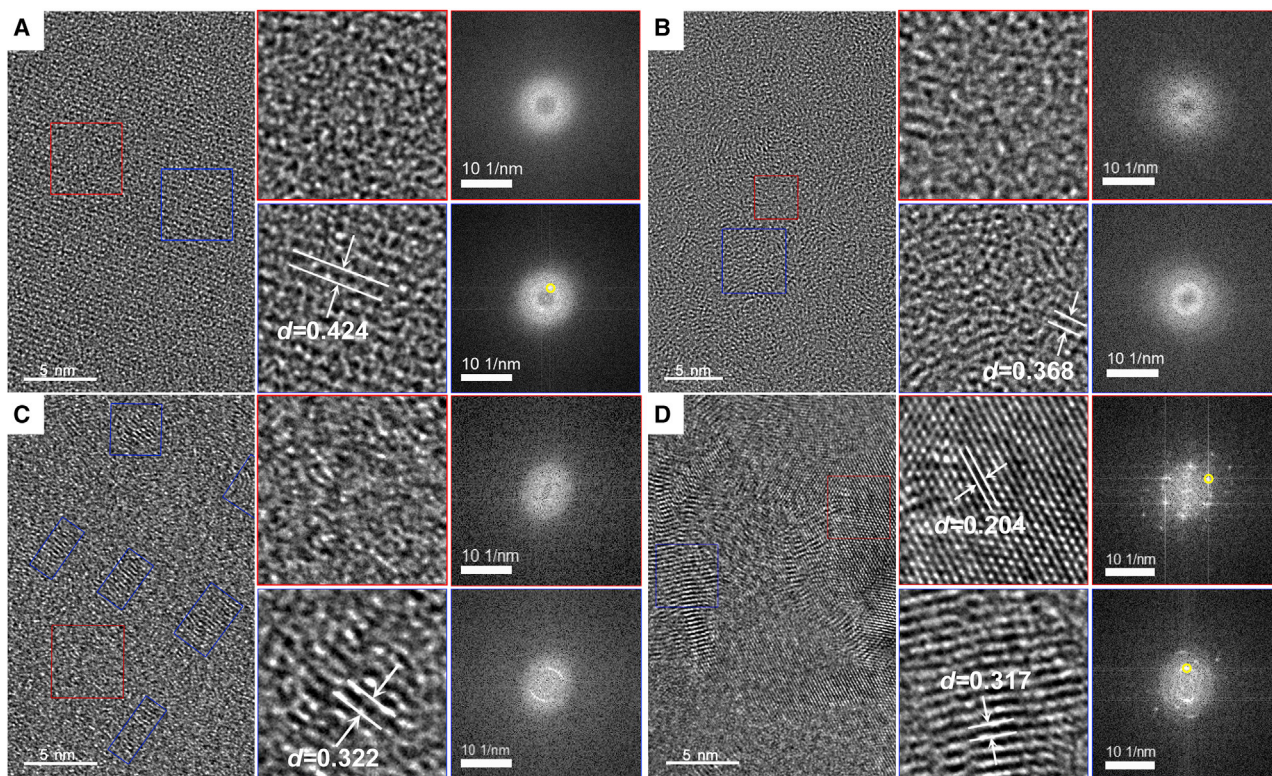
Figure 2. HRTEM images of samples 1, 3, 4, and 5

The figures on the right side of each panel include zoomed-in views of the square-marked areas in the HRTEM images and corresponding FFT patterns. The d spacing marked in the HRTEM images was estimated based on the corresponding spots (yellow) or halos in the FFT patterns.

(A) The crystalline periodicity of the residual 3D-C_{60} (blue box area) was interrupted by the amorphous components (red box area). The corresponding FFT patterns show the crystalline spots embedded in the amorphous halo.

(B) The am-I shows the completely disordered characteristics composed of fingerprint-like, small, curved nanographene fragments (blue box area) and the more-compact disordered structure (red box area). The corresponding FFT patterns in the two regions both exhibited diffused rings.

(C) The residual multilayer graphene clusters became ordered and oriented with reduced interlayer spacing (blue box area). The compact, disordered components in am-II were almost connected together (red box area). The corresponding FFT patterns also show the feature of being oriented in the multilayer graphene, and the interlayer diffraction signal has almost disappeared in the more-compact regions.

(D) The nanodiamond (red box area) and compressed graphite (blue box area) are clearly seen in the composite.

The microstructure of this composite nanostructured material was similar to that of natural impact diamonds and laboratory-synthesized diamond-related materials recently observed by HRTEM.[46–51] In these materials, the layered, graphite-like domains observed were non-periodically inserted and coherently connected to the sp^3-bonded diamond domains. Several interface-structure models of sp^2 (graphite-like) and sp^3 (diamond-like) units have been proposed to match the experimental HRTEM,[46–51] which would improve our understanding of complex nanostructures in diamond-related materials.

The sp^2 and sp^3 fractions of the am-I and am-II carbon materials were estimated by the carbon K-edge EELS spectra (Figure 3A). Compared with the low-loss EELS of raw C_{60} centered at 26.0 eV, the low-loss EELS of the two amorphous carbon materials right-shifted to 29.2 and 30.3 eV, respectively, indicating an increase in sp^3 bonding with increased synthesis temperature (Figure 3B). The plasmon energy was also a measure of density.[52] The densities of am-I and am-II converted from the plasmon peak-positions are 2.7 and 2.9 g/cm^3, respectively. These results were consistent with the measured results based on the Archimedes' principle
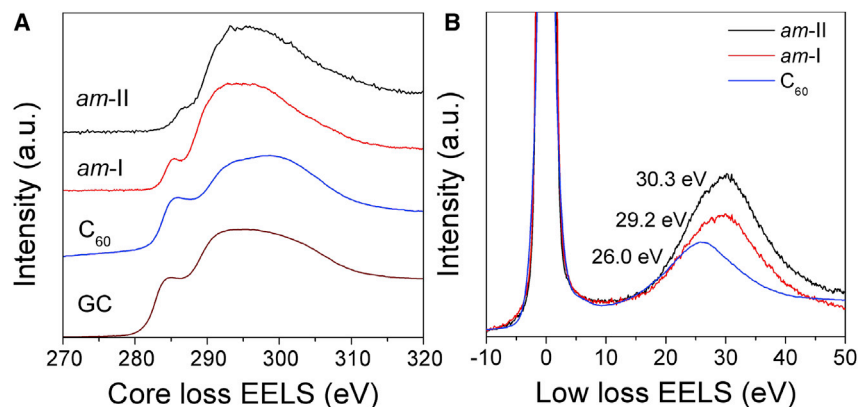
Figure 3. EELS spectra of raw C_{60} and resulting *am*-I and *am*-II samples

(A) The core loss EELS showed the decreased of sp^2 contribution in the *am*-I and *am*-II relative to the raw C_{60} and GC.

(B) The right shift of the plasmon peak in low-loss EELS spectra of *am*-I and *am*-II in comparison to the pristine C_{60} indicate an increased sp^3 fraction in structure.

(corresponding to 2.7 ± 0.1 and 3.0 ± 0.1 g/cm^3, respectively). The densities of *am*-I and *am*-II were less than that of diamond but greater than that ($\sim$2.0–2.5 g/cm^3) of the strong, hard, elastic, and conductive compressed glassy carbon with an sp^3 content up to 21%.[16] The core-loss EELS spectra displayed π^* and σ^* signatures, corresponding to the transition of 1 s to π^* and 1 s to σ^* in the amorphous carbon materials, respectively (Figure 3A). The π^* component decreased from the raw C_{60} to the amorphous carbon materials, also indicating an increase in the sp^3 carbon fraction. Using glassy carbon (GC) as a reference, the sp^3 content of *am*-I and *am*-II were estimated to be $50\% \pm 3\%$ and $63\% \pm 4\%$, respectively.

Structural model of the transformation

We conducted a systematic study of $C_{60} \rightarrow$ amorphous carbon transformation, which uncovered the mechanism that governed the material's evolution, which demonstrated that an increase in synthesis pressure required higher temperatures to set in the diffusion process in the system and driving a more-metastable "equilibrium" state after the buckyballs collapsed. Combined with the XRD, Raman, and HRTEM results, we propose the following phase-transformation process at a pressure of 15 GPa. When the synthesis temperature increased, the C_{60} molecular spheres would covalently bind to the nearest neighbors, forming the 3D-C_{60} polymer. Then, with further temperature increases and upon reaching the molecular-integrity threshold, the C_{60} spheres in the 3D-C_{60} polymer gradually collapsed into small fragments, forming the amorphous carbon (*am*-I) phase. There were two types of disordered structures in *am*-I, namely, disordered regions composed of short, fairly straight fragments, likely representing the fused aromatic rings (nanographene "seeds") grown from the collapsed C_{60}. In addition, there were denser, more-abundant disordered areas containing curled, tetrahedrally bonded carbon atoms, likely originating from the sp^3 linkages in the parent 3D-C_{60} polymer. With further increases in synthesis temperature, the short, curved fragments (the nanographene "seeds") merged into the more-ordered MLG clusters, $\sim$2 nm in lateral (in-plane) size. Then, as the temperature increased, they developed into 5–10 nm "thick" MLG stacks with lateral dimension of 5–10 nm. As they were more stable at high pressure, the compact, disordered regions rich in sp^3-bonded carbon gradually grew in volume, further densifying because of a continuous $sp^2 \rightarrow sp^3$ conversion and, finally, transforming into nanodiamond clusters.

Based on our current understanding of high p,T synthesis using fullerenes as a precursor, we propose an approach for designing novel amorphous carbon materials with controllable disorder. Specifically, in the class of systems considered, the disorder originated in the interaction between different types of short-range order in the two-phase system. For example (at 15 GPa), the "all-sp^2" structural units (short chains, fused aromatic rings, and graphene nanoclusters) embedded into the denser disordered matrix with a high concentration of sp^3 sites (the second component/phase). The possibility of chemically tuning the sp^2/sp^3 ratio in the latter by altering the synthesis p,T offers a large variety of structural scenario or metastable phases with promising combinations of physicochemical properties to be explored. In this regard, moving to pressure high enough to prevent the nanographene clusters formation/growth from the aromatic rings created when buckyballs collapse and, simultaneously, to promote $sp^2 \rightarrow sp^3$ carbon conversion, further enriching the surrounding dense, disordered matrix with sp^3 species, is undoubtedly the most intriguing and promising pathway in the future pursuit of new bulk, nearly pure sp^3/tetragonally coordinated amorphous carbon materials with enhanced physical properties.

Mechanical properties

The hardness values of amorphous carbon materials produced at high p,T from C_{60}, as reported earlier, are still a controversial issue. The focus of the controversy centers around whether the hardness of amorphous carbon can surpass that of diamond.[15,21] To obtain reliable hardness data, we measured the hardness of *am*-I and *am*-II by employing three independent hardness testing methods. As shown in Figures 4A and S4, the asymptotic Vickers hardness (H_V) values of *am*-I and *am*-II were 68 ± 2 and 81 ± 4 GPa, respectively. The Knoop hardness (H_K) values also reached 43 ± 3 and 57 ± 1 GPa, respectively. The nano-indentation hardness (H_N) values obtained by applying load in the range of 1.96–4.9 N were 64 ± 2 and 76 ± 1 GPa, for *am*-I and *am*-II, respectively, which was in good agreement with the Vickers hardness results (Figure 4A). Therefore, the *am*-I and *am*-II samples exhibited hardness values equal to that of the (111) plane of single-crystal diamond.[53]

The Young's modulus (E) can be determined by the Oliver and Pharr method from the load/displacement curve during nano-indentation.[59] By assuming a Poisson's ratio of 0.2 for the materials, the E values of *am*-I and *am*-II obtained were 625 ± 7 GPa and 874 ± 24 GPa, respectively. The load-displacement curves also showed high-elasticity response to local deformation for the two samples, and elastic recovery after load release was $80 \pm 1\%$ and $69 \pm 1\%$, for *am*-I and *am*-II, respectively (Figure 4B). The high elasticity of the amorphous carbon materials was due to the disorder and flexibility of the nanometer-sized clusters, which comprised several graphene layers (see Figure 2). The existence of the fingerprint-like, curved microstructure of the former was possibly responsible for the material's higher elastic recovery.

The fracture toughness (K_{Ic}) of *am*-I and *am*-II was accurately determined from the cracks caused by Vickers indentation (Figures S6B and S6D). We found that the two amorphous carbon materials exhibited extremely high fracture-toughness values of 7.6 ± 0.6 and 8.0 ± 0.9 MPa · m$^{1/2}$, respectively (Figure 4C). These values are very unusual for amorphous materials that normally exhibit low fracture-toughness values of ~0.1–4.6 MPa · m$^{1/2}$.[54–58] Importantly, our results confirmed those determined earlier, with large uncertainly, high fracture-toughness valued (6.9–15.5 MPa·m$^{1/2}$) of amorphous carbon produced from C_{60} at a lower pressure of 12.5 GPa and moderate temperatures of 500–700°C.[30] A comparison of the fracture-toughness values of the
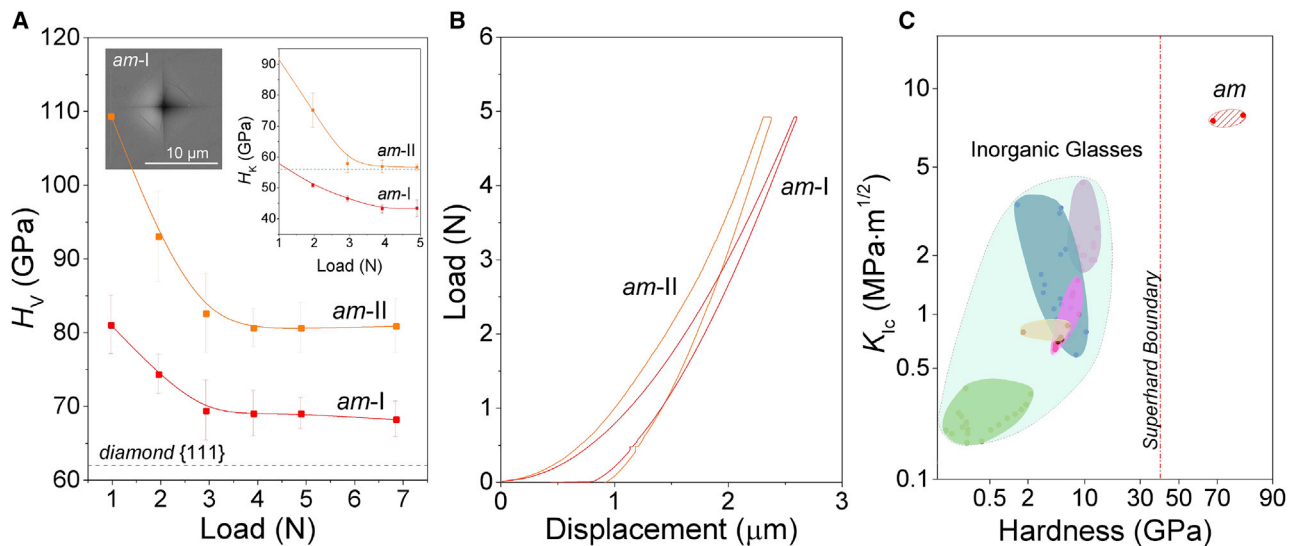
Figure 4. Mechanical properties of *am*-I and *am*-II

(A) Vickers hardness (H_V) of *am*-I and *am*-II as a function of the applied loads. At loads exceeding 2.94 N, the H_V approached the asymptotic value. Left panel inset: SEM image of the residual indentation made by the Vickers pyramid probe on the *am*-I surface after unloading from 4.9 N. Right panel inset: Knoop hardness (H_K) of *am*-I and *am*-II as a function of the applied loads. Error bars indicate SD (n = 5). The dashed lines denote the H_V and H_K of the (111) plane of natural diamond.[53]

(B) The load-displacement curves of *am*-I and *am*-II recorded during nanoindentation testing exhibited high elastic recovery.

(C) Comparison of hardness and fracture toughness between *am*s (current work) and ordinary inorganic glass, including silicate glass (dark cyan),[54] B_2O_3-based glass (magenta),[55] silicon oxynitride glass (yellow),[56] chalcogenide glass (green),[57] and SiO_2-based glass (purple).[58] For clarity, the data are represented by the probability function.

materials, with inorganic glass and ta-C films, is shown in Figure 4C. The ordinary silicate glass had a K_{Ic} value of only ~1 MPa · m$^{1/2}$,[54] whereas the K_{Ic} values for the a-Al_2O_3 films were 3.4 MPa · m$^{1/2}$.[60] Consequently, the amorphous carbon produced in this work had superior mechanical properties: a hardness on par with single-crystal diamond and fracture toughness comparable to that of Co-doped polycrystalline diamond.[28]

Electrical and optical properties

Currently, only one report in the literature addresses the electrical properties of amorphous carbon derived from fullerenes at p > 10 GPa, where a very low band gap (0.06–0.25 eV) was determined in the material recovered from high-pressure conditions at 12.5 GPa and 15 GPa.[24] However, only two temperatures (827°C and 1,527°C) were used during the synthesis at a pressure of 15 GPa. Therefore, in this study, we extended the synthesis temperature range similar to that in the Blank et al reference.[29] The temperature dependence of the resistivity of the *am*-I and *am*-II samples, ρ(T), exhibited behavior typical for semiconductor materials, and the resistivity decreased with increased temperature (Figure 5A). The room-temperature resistivity values were 19 and 35 ohm · cm for *am*-I and *am*-II, respectively, which was comparable to that of a polycrystalline Ge semiconductor (~40 ohm · cm).[61] Typically, for amorphous materials, it is difficult to accurately measure the intrinsic band gap. The temperature dependence of conductivity σ(T) provides a method to approximate the intrinsic band gap of semiconductors from the activation energy,[62] and σ(T) is defined by Equation 1:

$$\sigma(T) = \sigma_0 \exp\left(-\frac{E_g}{2K_B T} \right)$$

(Equation 1)
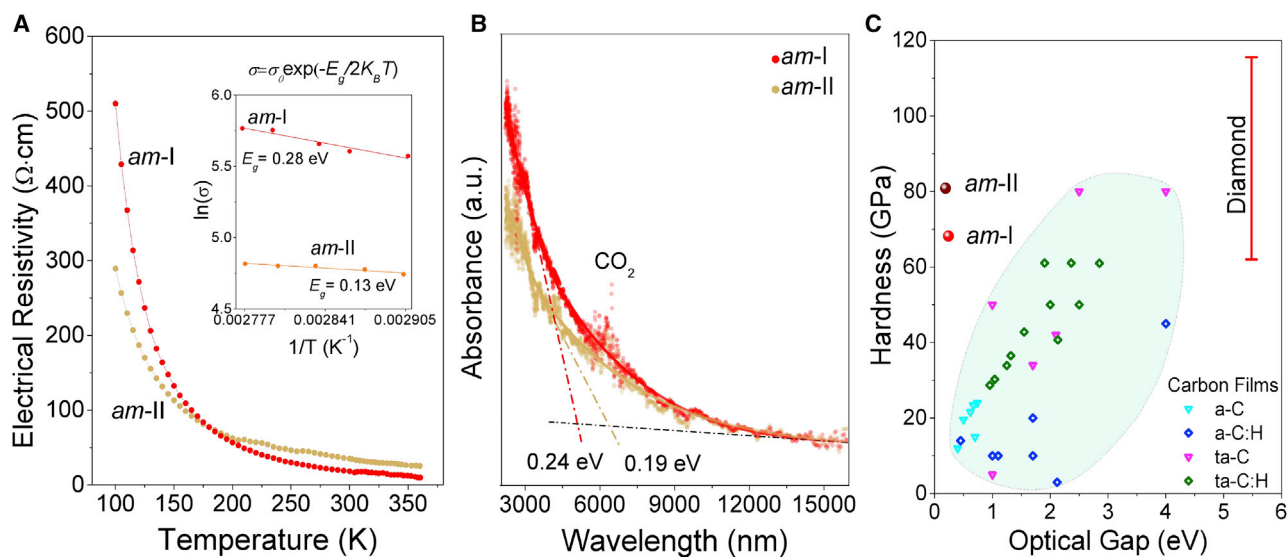
Figure 5. Electrical and optical properties of *am*-I and *am*-II

(A) Temperature dependence of the electrical resistivity showing the semiconductor behavior of *am*-I and *am*-II. Inset: activation energies obtained from the relationship of high-temperature conductivity. The estimated band gaps of *am*-I and *am*-II were 0.28 and 0.13 eV, respectively.

(B) FTIR-ATR spectra of *am*-I and *am*-II. The absorption edges of *am*-I and *am*-II were located at ~5,100 and ~6,500 nm, respectively, corresponding to Tauc gaps of 0.24 and 0.19 eV. The sharp peaks around ~6,400 nm was caused by CO_2 in the air.

(C) Hardness and optical gap of *am*-I and *am*-II in comparison with a-C(:H)/ta-C(:H) films[5,64,65] and single-crystal diamond.

where E_g is the band gap, σ_0 is a constant, and K_B is the Boltzmann's constant. By fitting the conductivity data in the high-temperature region of 360-340 K (Figure 5A), the band gaps of *am*-I and *am*-II were estimated to be 0.28 and 0.13 eV, respectively. Moreover, the Tauc gap provided a useful measure of the optical gap.[63] As shown in Figure 5B, the Tauc gap was determined directly from the absorption edge of the FTIR-ATR spectra, which were 0.24 and 0.19 eV for *am*-I and *am*-II, respectively. These results were consistent with the results obtained from the temperature-dependent resistivity. The narrow band gap formed was related to a component of the graphite-like, disordered structure in the amorphous carbon. With fewer disordered, graphite-like components and increased diamond-like compact components in the microstructure, the band gap of amorphous carbon was expected to increase.

The very narrow band gap observed in the synthesized amorphous materials is unusual for carbon systems. Diamond is an insulator with a large bandgap of 5.5 eV; however, graphene has a zero band gap and C_{60} is sp^2-type carbon that exhibits semiconducting behavior with a medium-sized band gap of ~1.5 eV. In addition, the 1D-, 2D-, 3D-polymerized C_{60} were mostly electron conductive,[13] and the hard ta-C(:H) films had optical gaps of 0.4–3 eV (Figure 5C).[5,64] However, the amorphous carbon materials synthesized in the bulk form had excellent mechanical properties, such as a hardness comparable to a single-crystal diamond and fracture toughness better than that of ordinary amorphous materials, with large indentation elastic recovery. In addition, they possessed a band-gap range extending down to ~0.19 eV. This range corresponds to the infrared photon-energy range, which covers not only the first atmospheric spectral window (~3–5 μm) in the mid-infrared but also extended to the second atmospheric spectral window (~8–14 μm) in the far-infrared portion of the spectrum. Consequently, these amorphous carbon materials are very promising materials for mid-far infrared radiation detection and energy harvesting.

In summary, this work studied the transformation of fullerene C_{60} at a high pressure of 15 GPa at various synthesis temperatures and clarified the microstructure and properties of the resulting bulk amorphous carbon materials. To our knowledge, this work is the most comprehensive and systematic study of the structural transformation of fullerene to amorphous carbon to date. For the first time, all transformation steps were followed through direct structural characterization on the nanometer scale via HRTEM. This allowed us to create a long-awaited, generalized structural-transformation model of $C_{60} \rightarrow$ amorphous carbon, to ascertain the inconsistency of previously published results, and to propose future development of amorphous carbon materials through high p,T synthesis. We showed that an increase in synthesis pressure required higher temperatures to set in the diffusion process of the system, which evolved into a metastable "equilibrium" state after the buckyball collapse. Consequently, the system's microstructural evolution, with increased synthesis temperature, determined the various physical properties of the resulting amorphous carbon materials. In particular, the amorphous carbon materials were actually narrow-band gap semiconductors with a band-gap value of only ∼0.1–0.3 eV. This class of amorphous carbon materials not only exhibited a diamond-like hardness but also had superior fracture toughness, which was comparable to that of Co-doped polycrystalline diamond.[28] This was very prominent in the amorphous system and was about eight times the fracture toughness of silicate glass.[54] These amorphous carbon materials, with excellent mechanical properties and narrow band gaps, could potentially be used in many fields. For example, they would be applicable as superhard and high-toughness tools and in unique/advanced photoelectric devices in which diamond and graphene are not suitable.[66] Based on our current understanding of high p,T synthesis using fullerene as the precursor, we proposed a different approach to the design of novel amorphous carbon materials with controllable disorder, compared with that of the packing disorder in layered sp^2/sp^3 polytypes.[49,50]

EXPERIMENTAL PROCEDURES

Resource availability

Lead contact

Information and requests for resources and materials should be directed to the lead contact, Zhisheng Zhao (zzhao@ysu.edu.cn).

Materials availability

All unique/stable reagents generated in this study are available from the lead contact with a completed materials transfer agreement.

Data and code availability

All data are reported in the paper or in the Supplemental information.

Sample synthesis

Samples were synthesized from fullerene C_{60} powder (99.99%, Alfa Aesar) using the standard COMPRES 10/5 assembly for HPHT experiments in a large-volume multi-anvil press at Yanshan University. The raw C_{60} powder was compacted and loaded into 2.0-mm (inner diameter) and 2.0-mm (height) h-BN capsules and was, then, assembled into a hole in the center of a 10-mm spinel ($MgAl_2O_4$) + MgO octahedron with an Re heater and an $LaCrO_3$ thermal insulator. Pressure loading/unloading rates were set to 2 GPa/h. Each sample was heated at a rate of 20°C/min to the peak temperature after the target pressure of 15 GPa was reached and then quenched to ambient T after holding the peak temperature for 2 h with subsequent pressure release. For each peak temperature (550°C, 700°C, 800°C, 1,000°C, and 1,200°C), a new sample was prepared, but the source fullerene material was removed from

the same batch. The dimensions of the specimens recovered reached $\sim$1.5–1.7 mm in diameter and $\sim$1.2–1.7 mm in height.

XRD and Raman spectroscopy

XRD spectra were obtained with a Bruker D8 Discover diffractometer (Cu $K\alpha$ radiation) from the recovered bulk samples.

The Raman spectra were collected at ambient conditions using a Horiba Jobin-Yvon LabRAM HR-Evolution Raman microscope. For excitation, 325-nm and 532-nm lasers were used, with the beam was focused on a spot of less than 2 μm in diameter on the sample surface. Special care was taken to avoid sample overheating during spectra collection.

HRTEM and EELS measurements

Microstructures of the recovered samples were characterized with a condenser, spherical-aberration-corrected TEM (Themis Z, Thermo Fisher Scientific) with an accelerating voltage of 300 kV and a TEM (Talos F200X) with an accelerating voltage of 200 kV. The specimens for HRTEM were prepared with Ga-focused ion beam (FIB, Scios Dual beam, Thermo Fisher Scientific) milling with an accelerating voltage of 30 kV from the bulk samples. To minimize the knockout damage of the specimens, ion cleaning was executed with a voltage of 5 kV and current of 16 pA for the electron-transparent slices and a thickness of less than 100 nm. EELS were collected in the TEM model from a randomly selected $\sim$200 nm region. The sp^3 ratio in the carbon samples was estimated from the carbon K-edge EELS method,[16] and glassy carbon was used as the reference.

Mechanical performance measurements

The hardness of the samples was investigated by obtaining three independent hardness measurements. The nanoindentation hardness (H_N) and Young's moduli (E) were derived from the load-displacement curves established by the three-sided pyramidal (Berkovich) diamond indenter (Nano Indenter G200). The applied loads ranged from 1.96 to 4.9 N, and the loading and dwelling times were both 15 s. The elastic recovery was calculated using the following formula:

$$\frac{d_{max} - d_{min}}{d_{max}} \qquad \text{(Equation 2)}$$

where d_{max} and d_{min} are the maximum displacement at maximum load and the residual after unloading, respectively. The Knoop (H_K) and Vickers (H_V) hardness measurements were carried out on the microhardness tester (KB 5 BVZ), and the adopted loading and dwelling times were 30 and 15 s, respectively. H_K was determined from Equation 3:

$$H_K = \frac{14,229P}{d_1^2} \qquad \text{(Equation 3)}$$

where P (N) is the applied load and d_1 (μm) is the major diagonal length (long axis) of the rhomboid-shaped Knoop indentation. H_V was determined from Equation 4:

$$H_V = \frac{1,854.4P}{d_2^2} \qquad \text{(Equation 4)}$$

where d_2 (in micrometers) is the arithmetic mean of the two diagonals of the Vickers indentation. The loads applied during H_V and H_K measurements were in the range of 0.98–6.86 N. For each test method, for each sample, at least five indentations were used at different loads. All hardness values were determined from the scanning electron microscopy (SEM) images of the indentations. The fracture toughness (K_{Ic}) was also

estimated from the Vickers indentation cracks, which were produced at a load of 6.68 N. The value from the radial cracks formed on surfaces of bulk samples was calculated by

$$K_{Ic} = 0.016 \left(\frac{E}{H_v} \right)^{0.5} \frac{F}{C^{1.5}}$$ (Equation 5)

where C (in micrometers) is the average length of the radial cracks measured from the indent center, and E is Young's modulus.

Electrical measurements

The electrical resistivity of the samples was measured at 100–360 K with a physical property measurement system (Quantum Design, USA), using the four-probe method. Platinum wires were adhered to the surface of the polished sample (~1.5 mm in diameter) with Leitsilber conductive silver cement (Ted Pella, silver content 45%).

Infrared absorption measurements

The FTIR-ATR was recorded in the spectral range of 600–4,500 cm^{-1} (E55+FRA106, Bruker) from polished ~1.5-mm-diameter and 0.5-mm-thick samples under ambient conditions.

SUPPLEMENTAL INFORMATION

Supplemental information can be found online at https://doi.org/10.1016/j.xcrp.2021.100575.

AUTHOR CONTRIBUTIONS

Z.Z., A.V.S., and Y.T. conceived the idea for this project; S.Z., B.L., K.L., and L.S. prepared the samples; S.Z., Y.W., Y.S., Y.Z., and K.L. measured the XRD and Raman spectra; S.Z., Y.G., P.Y., and M.M. performed hardness measurements; S.Z., Y.W., and Y.S. scanned the indentations through the scanning electron microscope (SEM); S.Z. and B.L. measured the absorption spectra; K.L., S.Z., B.L., and Z.L. prepared the TEM samples using focused ion beam (FIB) technology; K.L., W.H., S.Z., Y.W., and Z.L. conducted TEM and EELS characterization; Z.Z., S.Z., A.V.S., J.H., D.Y., B.X., Y.T., V.B., O.P.C., K.L., W.H., Y.W., and Y.G. analyzed the data; and Z.Z., S.Z., and A.V.S drafted the manuscript with contributions from all authors.

DECLARATION OF INTERESTS

The authors claim that the patents for the current study have been granted in China (CN. 201910085279.0) and Japan (JP. 2020-009244).

REFERENCES

1. Schwierz, F. (2010). Graphene transistors. Nat. Nanotechnol. *5*, 487–496.

2. Denis, P.A. (2010). Band gap opening of monolayer and bilayer graphene doped with aluminium, silicon, phosphorus, and sulfur. Chem. Phys. Lett. *492*, 251–257.

3. Ke, F., Chen, Y., Yin, K., Yan, J., Zhang, H., Liu, Z., Tse, J.S., Wu, J., Mao, H.K., and Chen, B. (2019). Large bandgap of pressurized trilayer graphene. Proc. Natl. Acad. Sci. USA *116*, 9186–9190.

4. Zhang, Y., Tang, T.-T., Girit, C., Hao, Z., Martin, M.C., Zettl, A., Crommie, M.F., Shen, Y.R., and Wang, F. (2009). Direct observation of a widely tunable bandgap in bilayer graphene. Nature *459*, 820–823.

5. Robertson, J. (2002). Diamond-like amorphous carbon. Mater. Sci. Eng. R Rep. *37*, 129–281.

6. Luo, K., Liu, B., Sun, L., Zhao, Z.S., and Tian, Y.J. (2021). Design of a class of new sp^2–sp^3 carbons constructed by graphite and diamond building blocks. Chin. Phys. Lett. *38*, 028102.

7. Narayan, J., and Bhaumik, A. (2015). Novel phase of carbon, ferromagnetism, and conversion into diamond. J. Appl. Physiol. *118*, 215303.

8. Soldatov, A.V., Roth, G., Dzyabchenko, A., Johnels, D., Lebedkin, S., Meingast, C., Sundqvist, B., Haluska, M., and Kuzmany, H. (2001). Topochemical polymerization of C_{70} controlled by monomer crystal packing. Science *293*, 680–683.

9. McKenzie, D.R. (1996). Tetrahedral bonding in amorphous carbon. Rep. Prog. Phys. *59*, 1611–1664.

10. Bourdon, E.B.D., Duley, W.W., Jones, A.P., and Prince, R.H. (1991). Characterization of diamond-like films prepared by laser ablation of graphite. Surf. Coat. Technol. *47*, 509–516.

11. Dwivedi, N., Kumar, S., Malik, H.K., Govind, Rauthan, C.M.S., and Panwar, O.S. (2011). Correlation of sp^3 and sp^2 fraction of carbon with electrical, optical and nano-mechanical properties of argon-diluted diamond-like carbon films. Appl. Surf. Sci. *257*, 6804–6810.

12. Friedmann, T.A., Sullivan, J.P., Knapp, J.A., Tallant, D.R., Follstaedt, D.M., Medlin, D.L., and Mirkarimi, P.B. (1997). Thick stress-free amorphous-tetrahedral carbon films with hardness near that of diamond. Appl. Phys. Lett. *71*, 3820–3822.

13. Álvarez-Murga, M., and Hodeau, J.L. (2015). Structural phase transitions of C_{60} under high-pressure and high-temperature. Carbon *82*, 381–407.

14. Chernogorova, O., Potapova, I., Drozdova, E., Sirotinkin, V., Soldatov, A.V., Vasiliev, A., and Ekimov, E. (2014). Structure and physical properties of nanoclustered graphene synthesized from C_{60} fullerene under high pressure and high temperature. Appl. Phys. Lett. *104*, 043110.

15. Blank, V.D., Buga, S.G., Ivlev, A.N., and Mavrin, B.N. (1995). Ultrahard and superhard carbon phases produced from C_{60} by heating at high

pressure: structural and Raman studies. Phys. Lett. A *205*, 208–216.

16. Hu, M., He, J., Zhao, Z., Strobel, T.A., Hu, W., Yu, D., Sun, H., Liu, L., Li, Z., Ma, M., et al. (2017). Compressed glassy carbon: An ultrastrong and elastic interpenetrating graphene network. Sci. Adv. *3*, e1603213.

17. Zeng, Z., Yang, L., Zeng, Q., Lou, H., Sheng, H., Wen, J., Miller, D.J., Meng, Y., Yang, W., Mao, W.L., and Mao, H.K. (2017). Synthesis of quenchable amorphous diamond. Nat. Commun. *8*, 322.

18. Hu, M., Zhang, S., Liu, B., Wu, Y., Luo, K., Li, Z., Ma, M., Yu, D., Liu, L., Gao, Y., et al. (2021). Heat-treated glassy carbon under pressure exhibiting superior hardness, strength and elasticity. J. Materiomics *7*, 177–184.

19. Wood, R.A., Lewis, M.H., West, G., Bennington, S.M., Cain, M.G., and Kitamura, N. (2000). Transmission electron microscopy, electron diffraction and hardness studies of high-pressure and high-temperature treated C_{60}. J. Phys. Condens. Matter *12*, 10411–10421.

20. Chernogorova, O., Drozdova, E., Ovchinnikova, I., Soldatov, A.V., and Ekimov, E. (2012). Structure and properties of superelastic hard carbon phase created in fullerene-metal composites by high temperature-high pressure treatment. J. Appl. Phys. *111*, 112601.

21. Blank, V.D., Buga, S.G., Dubitsky, G.A., Serebryanaya, N.R., Popov, M.Y., and Sundqvist, B. (1998). High-pressure polymerized of C_{60}. Carbon *36*, 319–343.

22. Talyzin, A.V., Langenhorst, F., Dubrovinskaia, N., Dub, S., and Dubrovinsky, L.S. (2005). Structural characterization of the hard fullerite phase obtained at 13 GPa and 830 K. Phys. Rev. B Condens. Matter Mater. Phys. *71*, 115424.

23. Brazhkin, V.V., Lyapin, A.G., Popova, S.V., Voloshin, R.N., Antonov, Y.V., Lyapin, S.G., Kluev, Y.A., Naletov, A.M., and Mel'nik, N.N. (1997). Metastable crystalline and amorphous carbon phases obtained from fullerite C_{60} by high-pressure–high-temperature treatment. Phys. Rev. B Condens. Matter *56*, 11465–11471.

24. Buga, S.G., Blank, V.D., Serebryanaya, N.R., Dzwilewski, A., Makarova, T., and Sundqvist, B. (2005). Electrical properties of 3D-polymeric crystalline and disordered C_{60} and C_{70} fullerites. Diam. Relat. Mater *14*, 896–901.

25. Brazhkin, V.V., Lyapin, A.G., Lyapin, S.G., Popova, S.V., Voloshin, R.N., and Antonov, Y.A. (1998). Structural transformations in fullerite C_{60} under high-pressure (P=12.5 GPa) and high-temperature conditions. Rev. High Pressure Sci. Technol. *7*, 817–819.

26. Muhli, H., Chen, X., Bartók, A.P., Hernández-León, P., Csányi, G., Ala-Nissila, T., et al. (2021). Machine learning force fields based on local parametrization of dispersion interactions: Application to the phase diagram of C_{60}. arXiv. https://doi.org/10.1103/PhysRevB.104.054106.

27. Brazhkin, V.V., and Lyapin, A.G. (2012). Hard and superhard carbon phases synthesized from fullerites under pressure. J. Superhard Mater. *34*, 400–423.

28. Lammer, A. (1988). Mechanical properties of polycrystalline diamonds. Mater. Sci. Technol. *4*, 949–988.

29. Blank, V.D., Dubitsky, G.A., Serebryanaya, N.R., Mavrin, B.N., Denisov, V.N., Buga, S.G., and Chernozatonskii, L.A. (2003). Structure and properties of C_{60} and C_{70} phases produced under 15 GPa pressure and high temperature. Phys. B. Condens. Matter *339*, 39–44.

30. Brazhkin, V.V., Lyapin, A.G., Popova, S.V., Klyuev, Y.A., and Naletov, A.M. (1998). Mechanical properties of the 3D polymerized, sp^2–sp^3 amorphous, and diamond-plus-graphite nanocomposite carbon phases prepared from C_{60} under high pressure. J. Appl. Phys. *84*, 219–226.

31. Shibazaki, Y., Kono, Y., and Shen, G. (2019). Compressed glassy carbon maintaining graphite-like structure with linkage formation between graphene layers. Sci. Rep. *9*, 7531.

32. Álvarez-Murga, M., Bleuet, P., Garbarino, G., Salamat, A., Mezouar, M., and Hodeau, J.L. (2012). "Compressed graphite" formed during C_{60} to diamond transformation as revealed by scattering computed tomography. Phys. Rev. Lett. *109*, 025502.

33. Ferrari, A.C., and Robertson, J. (2000). Interpretation of Raman spectra of disordered and amorphous carbon. Phys. Rev. B Condens. Matter Mater. Phys. *61*, 14095–14107.

34. Ferrari, A.C., and Robertson, J. (2001). Resonant Raman spectroscopy of disordered, amorphous, and diamondlike carbon. Phys. Rev. B Condens. Matter Mater. Phys. *64*, 075414.

35. Ferrari, A.C., and Robertson, J. (2001). Origin of the 1150-cm^{-1} Raman mode in nanocrystalline diamond. Phys. Rev. B Condens. Matter Mater. Phys. *63*, 121405.

36. Bethune, D.S., Meijer, G., Tang, W.C., Rosen, H.J., Golden, W.G., Seki, H., Brown, C.A., and de Vries, M.S. (1991). Vibrational Raman and infrared spectra of chromatographically separated C_{60} and C_{70} fullerene clusters. Chem. Phys. Lett. *179*, 181–186.

37. Stein, I.Y., Constable, A.J., Morales-Medina, N., Sackier, C.V., Devoe, M.E., Vincent, H.M., and Wardle, B.L. (2017). Structure-mechanical property relations of non-graphitizing pyrolytic carbon synthesized at low temperatures. Carbon *117*, 411–420.

38. Mallet-Ladeira, P., Puech, P., Toulouse, C., Cazayous, M., Ratel-Ramond, N., Weisbecker, P., Vignoles, G.L., and Monthioux, M. (2014). A Raman study to obtain crystallite size of carbon materials: a better alternative to the Tuinstra–Koenig law. Carbon *80*, 629–639.

39. Smith, M.W., and Tu, K.N. (2016). Structural analysis of char by Raman spectroscopy: improving band assignments through computational calculations from first principles. Carbon *100*, 678–692.

40. Wang, Q., Wang, C., Wang, Z., Zhang, J., and He, D. (2007). Fullerene nanostructure-induced excellent mechanical properties in hydrogenated amorphous carbon. Appl. Phys. Lett. *91*, 141902.

41. Gupta, A.K., Tang, Y., Crespi, V.H., and Eklund, P.C. (2010). A non-dispersive Raman D-band activated by well-ordered interlayer interactions in rotationally stacked bi-layer graphene. Phys. Rev. B Condens. Matter Mater. Phys. *82*, 241406.

42. Milani, P., Ferretti, M., Piseri, P., Bottani, C.E., Ferrari, A., Li Bassi, A., et al. (1997). Synthesis and characterization of cluster-assembled carbon thin films. J. Appl. Phys. *82*, 5793–5798.

43. Hasdeo, E.H., Nugraha, A.R.T., Dresselhaus, M.S., and Saito, R. (2014). Breit-Wigner-Fano line shapes in Raman spectra of graphene. Phys. Rev. B Condens. Matter Mater. Phys. *90*, 245140.

44. Ribeiro-Soares, J., Oliveros, M.E., Garin, C., David, M.V., Martins, L.G.P., Almeida, C.A., Martins-Ferreira, E.H., Takai, K., Enoki, T., Magalhães-Paniago, R., et al. (2015). Structural analysis of polycrystalline graphene systems by Raman spectroscopy. Carbon *95*, 646–652.

45. Pimenta, M.A., Dresselhaus, G., Dresselhaus, M.S., Cançado, L.G., Jorio, A., and Saito, R. (2007). Studying disorder in graphite-based systems by Raman spectroscopy. Phys. Chem. Chem. Phys. *9*, 1276–1291.

46. Garvie, L.A.J., Nemeth, P., and Buseck, P.R. (2014). Transformation of graphite to diamond via a topotactic mechanism. Am. Mineral. *99*, 531–538.

47. Zhang, S., Zhang, Q., Liu, Z., Legut, D., Germann, T.C., Veprek, S., Zhang, H., and Zhang, R. (2020). Ultrastrong π-bonded interface as ductile plastic flow channel in nanostructured diamond. ACS Appl. Mater. Interfaces *12*, 4135–4142.

48. Xie, Y.-P., Zhang, X.-J., and Liu, Z.-P. (2017). Graphite to diamond: origin for kinetics selectivity. J. Am. Chem. Soc. *139*, 2545–2548.

49. Németh, P., McColl, K., Garvie, L.A.J., Salzmann, C.G., Murri, M., and McMillan, P.F. (2020). Complex nanostructures in diamond. Nat. Mater. *19*, 1126–1131.

50. Németh, P., McColl, K., Smith, R.L., Murri, M., Garvie, L.A.J., Alvaro, M., Pécz, B., Jones, A.P., Corà, F., Salzmann, C.G., and McMillan, P.F. (2020). Diamond-graphene composite nanostructures. Nano Lett. *20*, 3611–3619.

51. Zhu, S., Yan, X., Liu, J., Oganov, A.R., and Zhu, Q. (2020). A revisited mechanism of the graphite-to-diamond transition at high temperature. Matter *3*, 864–878.

52. Ferrari, A.C., Kleinsorge, B., Morrison, N.A., Hart, A., Stolojan, V., and Robertson, J. (1999). Stress reduction and bond stability during thermal annealing of tetrahedral amorphous carbon. J. Appl. Phys. *85*, 7191–7197.

53. Brookes, C.A., and Brookes, E.J. (1991). Diamond in perspective: a review of mechanical properties of natural diamond. Diam. Relat. Mater. *1*, 13–17.

54. Hand, R.J., and Tadjiev, D.R. (2010). Mechanical properties of silicate glasses as a function of composition. J. Non-Cryst. Solids *356*, 2417–2423.

55. Baik, D.S., No, K.S., Chun, J.S., Yoon, Y.J., and Cho, H.Y. (1995). A comparative evaluation method of machinability for mica-based glass-ceramics. J. Mater. Sci. *30*, 1801–1806.

56. Bauer, A., Christ, M., Zimmermann, A., and Aldinger, F. (2001). Fracture toughness of amorphous precursor-derived ceramics in the silicon-carbon-nitrogen system. J. Am. Chem. Soc. *84*, 5.

57. Guin, J.-P., Rouxel, T., Sanglebœuf, J.-C., Melscoët, I., and Lucas, J. (2002). Hardness, toughness, and scratchability of germanium-selenium chalcogenide glasses. J. Am. Chem. Soc. *85*, 1545–1552.

58. Rouxel, T., and Yoshida, S. (2017). The fracture toughness of inorganic glasses. J. Am. Ceram. Soc. *100*, 4374–4396.

59. Oliver, W.C., and Pharr, G.M. (1992). An improved technique for determining hardness and elastic modulus using load and displacement sensing indentation experiments. J. Mater. Res. *7*, 1564–1583.

60. Xia, Z., Riester, L., Sheldon, B.W., Curtin, W.A., Liang, J., Yin, A., and Xu, J.M. (2004). Mechanical properties of highly ordered nanoporous anodic alumina membranes. Rev. Adv. Mater. Sci. 6, 131–139.

61. Steele, M.C., and Rosi, F.D. (1958). Thermal conductivity and thermoelectric power of germanium-silicon alloys. J. Appl. Phys. *29*, 1517–1520.

62. Zhao, Z., Zhang, H., Kim, D.Y., Hu, W., Bullock, E.S., and Strobel, T.A. (2017). Properties of the exotic metastable ST12 germanium allotrope. Nat. Commun. *8*, 13909.

63. Tauc, J. (1974). Optical properties of amorphous semiconductor. In Amorphous and Liquid Semiconductors, J. Tauc, ed. (Springer), pp. 159–220.

64. Coşkun, Ö.D., and Zerrin, T. (2015). Optical, structural and bonding properties of diamond-like amorphous carbon films deposited by DC magnetron sputtering. Diam. Relat. Mater. *56*, 29–35.

65. Savvides, N. (1986). Optical constants and associated functions of metastable diamondlike amorphous carbon films in the energy range 0.5–7.3 eV. J. Appl. Phys. *59*, 4133–4145.

66. Chu, J., and Sher, A. (2010). Device Physics of Narrow Gap Semiconductors (Springer).